




Theory of modulation instability in Kerr Fabry-Perot resonators beyond the mean-field limit

Zoheir Ziani ^{1,*}, Thomas Bunel ¹, Auro M. Perego,² Arnaud Mussot,¹ and Matteo Conforti ^{1,†}

¹University of Lille, CNRS, UMR 8523-PhLAM Physique des Lasers, Atomes et Molécules, F-59000 Lille, France

²Aston Institute of Photonic Technologies, Aston University, Birmingham B4 7ET, United Kingdom



(Received 25 September 2023; accepted 12 December 2023; published 16 January 2024)

We analyze the nonlinear dynamics of Fabry-Perot cavities of arbitrary finesse filled by a dispersive Kerr medium, pumped by a continuous-wave laser or a synchronous train of flat-top pulses. The combined action of feedback, group velocity dispersion, and Kerr nonlinearity leads to temporal instability with respect to perturbations at specified frequencies. We characterize the generation of new spectral bands by deriving the exact dispersion relation, and we find approximate analytical expressions for the instability threshold and gain spectrum of modulation instability (MI). We show that, in contrast to ring resonators, both the stationary solutions and the gain spectrum are significantly affected by the duration of the pump pulse. We derive the extended Lugiato-Lefever equation for the Fabry-Perot resonator (FP-LLE) starting from coupled nonlinear Schrödinger equations, and we compare the outcome of the stability analysis of the two models. While FP-LLE gives overall good results, we show regimes that are not captured by the mean-field limit, namely, the period-two modulation instability, which may appear in highly detuned or nonlinear regimes. We report numerical simulations of the generation of MI-induced Kerr combs by solving FP-LLE and the coupled Schrödinger equations.

DOI: [10.1103/PhysRevA.109.013507](https://doi.org/10.1103/PhysRevA.109.013507)

I. INTRODUCTION

Optical cavities have been a valuable tool for studying various nonlinear effects since the invention of lasers in the 1960s. Bistability, self-pulsing, and modulation instability are some examples of these effects that have been observed experimentally and analyzed theoretically [1]. Most of the early theoretical studies were focused on ring cavities, where the light propagates only in one direction, simplifying considerably the analysis [2].

Nonetheless, Fabry-Perot (FP) cavities, where two distinct fields propagate simultaneously in the forward and backward directions, are exploited in many applications. Nonlinear interaction of counterpropagating fields can lead to very complex dynamics, even in the absence of a cavity. For instance, it has been demonstrated that counterpropagation and nonlinearity can cause transverse spatial [3–7] and temporal instabilities [8,9]. In resonators, temporal instabilities may appear even in the absence of group velocity dispersion (GVD), and they were first studied in a ring cavity (the well-known Ikeda instability) [2] and later in FP systems [10–12]. Despite several attempts, dispersive instabilities [or temporal modulation instability (MI)] in FP cavities are not completely characterized yet [13–15]. A complete theoretical analysis has been developed only in the good-cavity (also called mean-field) approximation. A version of the Lugiato-Lefever equation (also known as the driven-damped nonlinear Schrödinger equation [16]) generalized to FP resonators (FP-LLE) has been derived, which permits to identify

the peculiarity of the FP case in an additional detuning term depending on the average field power [17]. Beyond the mean-field limit, analytical expressions of the MI threshold have been obtained for a specific resonator where one of the mirrors has reflectivity equal to one [15].

The pioneering work on optical frequency combs (OFCs) by Braje *et al.* [18] and subsequent research by Obrzud *et al.* [19] in fiber-based FP cavities have opened up a new field of research focused on the generation and manipulation of OFCs [20–26]. They offer a high degree of flexibility in terms of comb bandwidth and mode spacing. However, despite the advantages of using FP cavities to produce OFCs, the experimental results are often poorly understood due to the lack of available analytical treatments. The ongoing efforts in this field aim at improving the understanding of the physics of OFCs and pave the way for their broader use in a variety of applications.

The goal of this paper is to describe MI in a nonlinear FP cavity with an instantaneous Kerr nonlinearity, second-order GVD, arbitrary mirror reflectivity, and arbitrary detuning. We derive the full complex dispersion relation for the perturbations, which permits to calculate the *exact* MI gain spectrum. We provide simpler but extremely accurate formulas of the MI gain, which extend the recent results reported in Ref. [15]. We compare the outcomes of our analysis with the prediction of the mean-field approximation, and report numerical simulations of MI comb generation in fiber FP resonators. The paper is organized as follows. In Sec. II, we review the basic equations that describe FP cavities and derive the expression for the stationary solutions. Then, in Sec. III, we perform a linear stability analysis and obtain the exact dispersion relation. Using appropriate approximations, we determine the gain spectrum that characterizes the modulation instability of

*ziani.zoheir@gmail.com

†matteo.conforti@univ-lille.fr

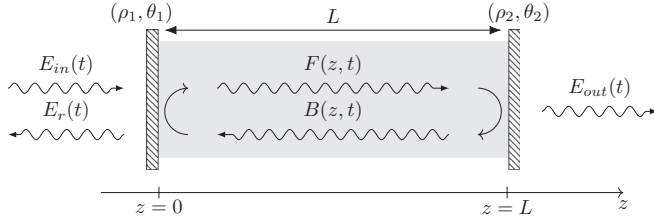


FIG. 1. Schematic diagram of a nonlinear FP cavity of arbitrary finesse located in the interval $0 \leq z \leq L$.

homogeneous solutions. In Sec. IV, we study the effect of the pulsed pump on the system response. Finally, in Sec. V, we show some typical examples where mean-field approximation breaks down. Conclusions are drawn in Sec. VI.

II. FABRY-PEROT CAVITY DESCRIPTION

We consider a FP cavity of length L , filled with a nonlinear Kerr medium (see Fig. 1). A pump field E_{in} enters at $z = 0$ through a mirror of reflectivity ρ_1 and drives forward $F(z, t)$ and backward $B(z, t)$ fields in the cavity. A transmitted field E_{out} exits the cavity through the second mirror of reflectivity ρ_2 at $z = L$. The evolution of the two counterpropagating waves is described by a set of two coupled nonlinear Schrödinger equations (NLSEs) [10,15]:

$$\frac{\partial F}{\partial z} + \beta_1 \frac{\partial F}{\partial t} + i \frac{\beta_2}{2} \frac{\partial^2 F}{\partial t^2} = i\gamma(|F|^2 + G|B|^2)F, \quad (1a)$$

$$-\frac{\partial B}{\partial z} + \beta_1 \frac{\partial B}{\partial t} + i \frac{\beta_2}{2} \frac{\partial^2 B}{\partial t^2} = i\gamma(|B|^2 + G|F|^2)B, \quad (1b)$$

where $\beta_1^{-1} = v_g$ is the group velocity, β_2 is the group-velocity dispersion coefficient, γ is the nonlinear parameter, and $G = 2$ is the grating parameter which describes cross-phase modulation (XPM). We neglected the transverse spatial dependence of the envelopes, which applies for (i) plane waves or (ii) single-mode guides, like optical fibers. The governing equations are supplemented with appropriate boundary conditions at the left and right mirrors:

$$F(0, t) = \theta_1 E_{\text{in}}(t) + \rho_1 B(0, t), \quad (2a)$$

$$B(L, t) = \rho_2 e^{i\phi_0} F(L, t), \quad (2b)$$

where the linear cavity phase ϕ_0 accounts for the phase acquired during the propagation $2\beta_0 L$ (β_0 is the propagation constant) and any possible contribution from the mirrors, modulo 2π . Thus $-\pi \leq \phi_0 \leq \pi$, and we can introduce the cavity detuning as $\delta = -\phi_0$. The transmitted field E_{out} may be expressed as

$$E_{\text{out}}(t) = \theta_2 F(L, t). \quad (3)$$

Thereafter, we assume that the reflectivity and the transmissivity of the mirrors are real and verify $\theta_{1,2}^2 + \rho_{1,2}^2 = 1$. By taking $G = 0$ and $\rho_2 = 1$, Eqs. (1) and (2) model a ring cavity of length $2L$.

Equations (1a)–(2b) have continuous-wave (time-independent) solutions which are obtained by setting the

time derivatives in Eqs. (1) equal to zero and $E_{\text{in}}(t)$ constant [10,14,15,27]. They are of the form

$$F(z) = F_0 e^{+i\gamma(|F_0|^2 + G|B_0|^2)z} \equiv F_0 e^{i\phi_F z}, \quad (4a)$$

$$B(z) = B_0 e^{-i\gamma(|B_0|^2 + G|F_0|^2)z} \equiv B_0 e^{i\phi_B z}. \quad (4b)$$

Using Eqs. (2) we find

$$F_0 = \frac{\theta_1 E_{\text{in}}}{1 - \rho_1 \rho_2 \exp[i(\phi_0 + \phi_{NL})]}, \quad (5a)$$

$$B_0 = \rho_2 \exp[i(\phi_0 + \phi_{NL})] F_0, \quad (5b)$$

where the nonlinear phase is given by

$$\phi_{NL} = \gamma(1 + \rho_2^2)(1 + G)L|F_0|^2. \quad (6)$$

From Eqs. (5) we obtain the input power $P_{\text{in}} = |E_{\text{in}}|^2$ as a function of the intracavity forward power $P_F = |F_0|^2$:

$$P_{\text{in}} = \frac{P_F}{\theta_1^2} (1 + (\rho_1 \rho_2)^2 - 2\rho_1 \rho_2 \cos(\phi_0 + \phi_{NL})). \quad (7)$$

From Eq. (7) we find that the cavity finesse, i.e., the ratio between the linewidth and the free spectral range (FSR), is given by $\mathcal{F} = \frac{\pi\sqrt{\rho_1 \rho_2}}{1 - \rho_1 \rho_2}$.

III. LINEAR STABILITY ANALYSIS

A. General dispersion relation

The stability of the steady state is examined assuming a time-dependent solution of the form

$$F(z, t) = F_0(1 + f(z, t))e^{i\phi_F z}, \quad (8a)$$

$$B(z, t) = B_0(1 + b(z, t))e^{i\phi_B z}, \quad (8b)$$

where f and b are small perturbations. The linearized propagation equations for the perturbations read as

$$\frac{\partial f}{\partial z} + \beta_1 \frac{\partial f}{\partial t} + i \frac{\beta_2}{2} \frac{\partial^2 f}{\partial t^2} = 2i\gamma P_F \text{Re}(f + \rho_2^2 G b), \quad (9a)$$

$$-\frac{\partial b}{\partial z} + \beta_1 \frac{\partial b}{\partial t} + i \frac{\beta_2}{2} \frac{\partial^2 b}{\partial t^2} = 2i\gamma P_F \text{Re}(G f + \rho_2^2 b), \quad (9b)$$

where Re stands for the real part. From Eqs. (2), we find the following boundary conditions for f and b :

$$f(0, t) = \rho_1 \rho_2 e^{i\phi} b(0, t), \quad (10a)$$

$$f(L, t) = b(L, t), \quad (10b)$$

where $\phi = \phi_0 + \phi_{NL}$ is the total (linear plus nonlinear) phase shift. We write the perturbation in the following form:

$$f(z, t) = f_+(z)e^{\lambda t} + f_-^*(z)e^{\lambda^* t}, \quad (11a)$$

$$b(z, t) = b_+(z)e^{\lambda t} + b_-^*(z)e^{\lambda^* t}. \quad (11b)$$

The real and imaginary parts of $\lambda = \sigma + i\omega$ define the temporal growth rate and the frequency of the perturbations. By inserting Eqs. (11) in Eqs. (9), we find that the four complex amplitudes f_{\pm} , b_{\pm} of the perturbations obey the following system of ordinary differential equations:

$$\frac{d}{dz} \begin{pmatrix} f_+(z) \\ f_-(z) \\ b_+(z) \\ b_-(z) \end{pmatrix} = \mathcal{M} \begin{pmatrix} f_+(z) \\ f_-(z) \\ b_+(z) \\ b_-(z) \end{pmatrix}, \quad (12)$$

where

\mathcal{M}

$$= i\gamma P_F \begin{pmatrix} 1 + i\frac{\psi_+}{\gamma P_F} & 1 & G\rho_2^2 & G\rho_2^2 \\ -1 & -1 + i\frac{\psi_-}{\gamma P_F} & -G\rho_2^2 & -G\rho_2^2 \\ -G & -G & -\rho_2^2 - i\frac{\psi_+}{\gamma P_F} & -\rho_2^2 \\ G & G & \rho_2^2 & \rho_2^2 - i\frac{\psi_-}{\gamma P_F} \end{pmatrix},$$

with $\psi_{\pm} = \beta_1 \lambda \pm i\frac{\beta_2}{2} \lambda^2$. The growth rate σ and the frequency ω of the perturbations are found by imposing the following boundary conditions:

$$f_{\pm}(L) = b_{\pm}(L), \quad (13a)$$

$$f_{\pm}(0) = \rho_1 \rho_2 e^{\pm i\phi} b_{\pm}(0). \quad (13b)$$

The matrix differential equation (12) is linear and homogeneous, so it can be solved by standard methods (e.g., matrix exponential). However, the analytic expressions are very cumbersome since they depend on the roots of a general fourth-order polynomial. We report here the main passages, while theory derivation is reported in Appendix A. The solution of Eqs. (12) can be expressed in terms of eigenvalues and eigenvectors of \mathcal{M} :

$$(f_+, f_-, b_+, b_-)^T = \sum_{j=1}^4 c_j e^{\eta_j z} \mathbf{u}_j, \quad (14)$$

where $\mathbf{u}_j = (u_{j,1}, u_{j,2}, u_{j,3}, u_{j,4})^T$ are the eigenvectors of \mathcal{M} . The four arbitrary constants c_j are determined by the boundary conditions. Indeed, by inserting Eq. (14) in Eq. (13), we obtain a system of algebraic equations $\mathcal{N}(c_1, c_2, c_3, c_4)^T = 0$, where \mathcal{N} is defined in Eq. (A3). In order to have a nontrivial solution, we must impose $\det \mathcal{N} = 0$, which yields Eq. (A4). The dispersion relation $\det \mathcal{N} = 0$ is a complicated nonlinear equation in the complex variable $\lambda = \sigma + i\omega$. Even if we are not able to solve it analytically, it can be solved numerically [28]. Its solutions in the complex λ plane give the growth rate and the frequency of the possibly unstable perturbations.

B. Approximate solutions

The solution of Eqs. (12) is greatly simplified if $\beta_2 = 0$ or if $G = 0$. For the dispersionless case, we obtain the same results of Firth [10] (calculation not reported here). For the dispersive case, in order to achieve reasonably simple analytical expressions, we assume $G = 0$ in Eqs. (12) only. It amounts to suppressing the linear coupling between the perturbation components in the propagation equations. The reason for that is that the walk-off arising from counterpropagation weakens the XPM terms. Nonetheless, the coupling is maintained in the boundary conditions via the total phase ϕ . This approximation is physically sound: the main coupling between forward and backward perturbations takes place at the mirrors. We also maintain $G \neq 0$ in the steady state, meaning that the perturbations propagate on top of the correct steady state. Following similar arguments, the same approximation was used in Refs. [13–15]. Indeed, it has been shown that XPM is negligible if the mirrors provide the dominant coupling between forward and backward waves, which is generally the case in FP resonators [13].

Solving Eqs. (12) with $G = 0$ and using the same approach as before, we find the following characteristic equation:

$$e^{2\lambda t_R} - \Delta(\lambda) e^{\lambda t_R} + (\rho_1 \rho_2)^2 = 0, \quad (15)$$

where $t_R = 2\beta_1 L$ is the round-trip time and

$$\Delta(\lambda) = \rho_1 \rho_2 [a(\lambda) \cos \phi + b(\lambda) \sin \phi]$$

with

$$a(\lambda) = 2 \cos(kL) \cos(k_\rho L) - \frac{k^2 + k_\rho^2}{kk_\rho} \sin(kL) \sin(k_\rho L),$$

$$b(\lambda) = \frac{4k^2 + \beta_2^2 \lambda^4}{2\beta_2 \lambda^2 k} \cos(k_\rho L) \sin(kL)$$

$$+ \frac{4k_\rho^2 + \beta_2^2 \lambda^4}{2\beta_2 \lambda^2 k_\rho} \cos(kL) \sin(k_\rho L),$$

and

$$k^2 = \frac{\beta_2 \lambda^2}{2} \left(\frac{\beta_2 \lambda^2}{2} - 2\gamma P_F \right),$$

$$k_\rho^2 = \frac{\beta_2 \lambda^2}{2} \left(\frac{\beta_2 \lambda^2}{2} - 2\gamma P_F \rho_2^2 \right). \quad (16)$$

Even if the structure of Eq. (15) appears to be quite simple, it may admit an infinite number of solutions, since the discriminant depends on λ . We may also remark that Eq. (15) is equivalent to the following two equations:

$$e^{\lambda t_R} = \frac{\Delta(\lambda)}{2} \pm \sqrt{\frac{\Delta^2(\lambda)}{4} - (\rho_1 \rho_2)^2}. \quad (17)$$

From the analysis of the dispersionless case [10], we have learned that $\omega t_R = m\pi$ at threshold ($\sigma = 0$). It is worth noting that the frequencies of the perturbations at threshold correspond either to cavity resonances (m even) or they are in between (m odd, antiresonance). For $\sigma = 0$, Eq. (15) reads as

$$1 - (-1)^m \Delta + (\rho_1 \rho_2)^2 = 0, \quad (18)$$

which gives the analytic threshold expression

$$\tilde{a}(\omega) \cos \phi + \tilde{b}(\omega) \sin \phi = (-1)^m \frac{1 + (\rho_1 \rho_2)^2}{\rho_1 \rho_2}, \quad (19)$$

where $\tilde{a}(\omega) = a(\lambda = i\omega)$ and $\tilde{b}(\omega) = b(\lambda = i\omega)$. By taking $\rho_2 = 1$, we recover the main result of Ref. [15] in which the authors used the gain-circle method to find the threshold formula for the zero-transmission case.

Numerical solution of Eq. (15) shows that $\omega t_R \approx m\pi$ approximately holds even when $\sigma \neq 0$ with great precision. Moreover, we may assume that the frequency of the perturbation is much greater than its growth rate, i.e., $\omega \gg \sigma$. We thus write Eq. (15) in the form

$$e^{2\sigma t_R} - (-1)^m \tilde{\Delta}(\omega) e^{\sigma t_R} + (\rho_1 \rho_2)^2 = 0, \quad (20)$$

with $\tilde{\Delta}(\omega) = \Delta(\lambda = 0 + i\omega)$.

It is now straightforward to calculate the growth rate of the perturbations as a function of the frequency, i.e., $\sigma(\omega)$:

$$e^{\sigma t_R} = (-1)^m \frac{\tilde{\Delta}(\omega)}{2} \pm \sqrt{\frac{\tilde{\Delta}^2(\omega)}{4} - (\rho_1 \rho_2)^2}. \quad (21)$$

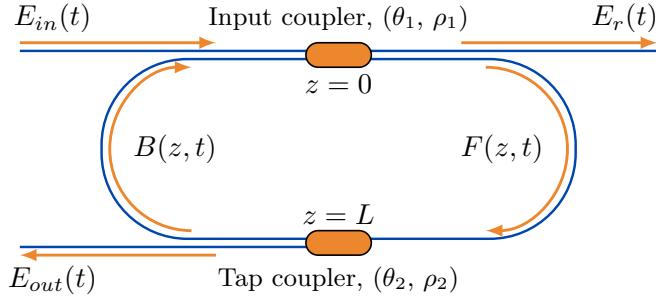


FIG. 2. The Fabry-Perot cavity of Fig. 1 in the limit $G = 0$ is equivalent to a ring cavity composed of two identical pieces of fibers of length L connected by two couplers (θ_1, ρ_1) and (θ_2, ρ_2) .

In order to observe MI, we must have $\sigma > 0$, so we have the following conditions:

$$(-1)^m \tilde{\Delta}(\omega) > 1 + (\rho_1 \rho_2)^2 \quad (22)$$

and

$$\sigma t_R = \ln \left((-1)^m \frac{\tilde{\Delta}}{2} + \sqrt{\frac{\tilde{\Delta}^2}{4} - (\rho_1 \rho_2)^2} \right). \quad (23)$$

We can define the MI gain $g(\omega)$ as the spatial growth rate:

$$g(\omega) = \frac{\sigma t_R}{2L} = \frac{1}{2L} \ln \max \left| \frac{\tilde{\Delta}}{2} \pm \sqrt{\frac{\tilde{\Delta}^2}{4} - (\rho_1 \rho_2)^2} \right|. \quad (24)$$

We recognize in Eq. (24) the MI gain of a ring cavity of length $2L$ composed of two identical pieces of fiber of length L [29] connected by an input coupler (θ_1, ρ_1) , and a tap coupler (θ_2, ρ_2) as illustrated in Fig. 2 (see Appendix B for details).

We verified that the approximation in Eq. (24) is extremely precise. As an example, we report in Fig. 3 the comparison between the exact and the approximated MI gain for a fiber FP resonator with an anomalous dispersion fiber and operating in the monostable regime (parameters are reported in the figure caption). Figure 3(a) shows the steady-state curve of Eq. (7), the working point being denoted with a red star. Figure 3(b) shows the approximated MI gain from Eq. (24) (blue curve) and the exact gain from numerical solution of Eq. (A4) (black circles). The circles are perfectly superposed to the continuous line: there is no visible difference between the two models. Indeed, we have found that for all our tests the exact and the approximated models give essentially identical results. Of course, the approximated model does not predict the frequencies of the perturbations, because here ω is a continuous, independent variable.

Two examples of the graphical solution of Eq. (A4) are shown in Figs. 3(c) and 3(d). Blue and red curves represent $\text{Re}(\det \mathcal{N}) = 0$ and $\text{Im}(\det \mathcal{N}) = 0$ in the complex λ plane. As a general feature, the curve $\text{Im}(\det \mathcal{N}) = 0$ is essentially composed of a horizontal line with $\sigma < 0$ and a set of vertical lines at $\omega t_R \approx m\pi$. The solutions are marked by solid black dots. Figure 3(c) shows two solutions with $\sigma < 0$, meaning that the perturbations at the corresponding frequency ω are stable, whereas Fig. 3(d) shows two solutions which share almost the same frequency (they are slightly different and very close to a cavity resonance $\omega t_R = 2m\pi$) but opposite σ . The

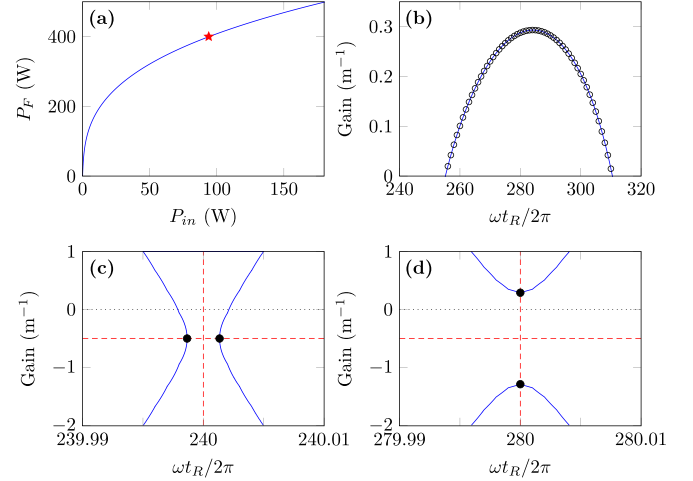


FIG. 3. (a) Intracavity forward power as a function of pump power from Eq. (7). (b) Approximated MI gain $g(\omega)$ from Eq. (24) (blue curve) and exact gain from numerical solution of Eq. (A4) (black circles). (c) Real (blue curve) and imaginary (red dashed curve) part of Eq. (A4) outside the MI gain band. The intersections between the two curves (black circles) are the solutions of Eq. (A4). (d) Same as (c) but inside the MI gain band. Parameters: $\rho_1^2 = \rho_2^2 = 0.99$ ($\mathcal{F} = 312$), $\theta_1^2 = \theta_2^2 = 0.01$, $\gamma = 2 \text{ W}^{-1}/\text{km}$, $\beta_1 = c/1.5$, $\beta_2 = -20 \text{ ps}^2/\text{km}$, $L = 0.01 \text{ m}$, $\phi_0 = 0$, $P_{\text{in}} = 94 \text{ W}$, and $P_F = 400 \text{ W}$.

fact that one solution has $\sigma > 0$ implies that the perturbation at this frequency is unstable.

C. The good-cavity limit: FP-LLE

When the mirror reflectivities are high and the cavity detuning is small, it is possible to obtain a mean-field description of the dynamics, which generalizes the celebrated Lugiato-Lefever equation (LLE) originally derived for the ring resonators [30,31] to FP cavities. Cole *et al.* [17] derived this FP-LLE starting from Maxwell-Bloch equations, while Xiao *et al.* [24] also arrived at the same equation from coupled mode theory. In Appendix C, we report an alternative derivation of the FP-LLE, which uses the coupled NLSEs (1) as the starting point. Besides being more suited to fiber-based FP resonators, our derivation is more general as it considers unequal mirror reflectivities and pulsed pumping. The FP-LLE reads as

$$t_R \frac{\partial \psi}{\partial \tau} = (-\alpha + i\phi_0)\psi + \theta_1 E_{\text{in}}(t) + 2L \left[-i \frac{\beta_2}{2} \frac{\partial^2}{\partial t^2} + i\gamma |\psi|^2 + i\gamma \frac{G}{t_R} \int_{-t_R/2}^{t_R/2} |\psi|^2 dt \right] \psi, \quad (25)$$

where $\psi(\tau, t)$ is the field envelope inside the cavity, $\alpha = 1 - \rho_1 \rho_2$ is the cavity loss, $t \in [-t_R/2, t_R/2]$ denotes the fast time in one cavity round trip, and τ is a slow time.

The homogeneous solutions ψ_s are found by setting the derivatives in Eq. (25) equal to zero. We obtain that the power of the stationary solutions is given by the solutions of the cubic following equation:

$$\theta_1^2 P_{\text{in}} = P_s (\alpha^2 + (\phi_0 + 2\gamma L(1 + G)P_s)^2), \quad (26)$$

where $P_s = |\psi_s|^2$ and $P_{in} = |E_{in}|^2$. We can assume ψ_s real without loss of generality, which implies that the input field must be complex and can be written as

$$\theta_1 E_{in} = \psi_s(\alpha - i(\phi_0 + 2\gamma L(1 + G)P_s)). \quad (27)$$

To study the stability of these solutions, we perform a linear stability by considering a perturbed solution of the form $\psi(t, \tau) = \psi_s + \xi(\tau, t)$. Assuming $\xi \ll \psi_s$ small, we obtain

$$t_R \frac{\partial \xi}{\partial \tau} = (-\alpha + i\phi_0)\xi - iL\beta_2 \frac{\partial^2 \xi}{\partial t^2} + 2i\gamma LP_s \left((2 + G)\xi + \xi^* + \frac{G}{t_R} \int_{-t_R/2}^{t_R/2} (\xi + \xi^*) dt \right). \quad (28)$$

We now expand the perturbation over the cavity modes with time-varying amplitudes:

$$\xi(\tau, t) = \varepsilon_n(\tau)e^{i\omega_n t} + \varepsilon_{-n}(\tau)e^{-i\omega_n t}, \quad (29)$$

with $\omega_n = n2\pi/t_R$. The amplitudes of the modal perturbations obey

$$t_R \frac{d\varepsilon_n}{d\tau} = (-\alpha + i\phi_0)\varepsilon_n + iL\beta_2 \omega_n^2 \varepsilon_n + 2i\gamma LP_s((2 + G)\varepsilon_n + \varepsilon_{-n}^*) + 2i\gamma LP_s G(\varepsilon_n + \varepsilon_{-n}^*)\delta_{n0}, \quad (30a)$$

$$t_R \frac{d\varepsilon_{-n}^*}{d\tau} = (-\alpha - i\phi_0)\varepsilon_{-n}^* + iL\beta_2 \omega_n^2 \varepsilon_{-n}^* - 2i\gamma LP_s((2 + G)\varepsilon_{-n}^* + \varepsilon_n) - 2i\gamma LP_s G(\varepsilon_n + \varepsilon_{-n}^*)\delta_{n0}, \quad (30b)$$

where δ_{n0} is the Kronecker delta. The last terms in Eqs. (30), which appear only for the zero mode, stem from the integral term which does not average to zero as in the case $n \neq 0$. This contribution is not present for the ring cavity, for which $G = 0$. The system (30) can be written as $d/d\tau(\varepsilon_n, \varepsilon_{-n}^*)^T = M_n(\varepsilon_n, \varepsilon_{-n}^*)^T$, and the eigenvalues of the matrix M_n determine the stability of the solution. The temporal growth rate of the perturbations for $n \neq 0$ reads

$$\sigma(\omega_n) = \frac{1}{t_R}(-\alpha + \sqrt{(2\gamma LP_s)^2 - \mu_n^2}), \quad (31)$$

where $\mu_n = \phi_0 + L\beta_2 \omega_n^2 + 2(2 + G)\gamma LP_s$. The temporal growth can be written as a spatial gain as $g(\omega_n) = \beta_1 \sigma(\omega_n)$. The most unstable mode, obtained for $\mu_n = 0$, and its growth rate are

$$\omega_n^2 = -\frac{\phi_0 + 2(2 + G)\gamma LP_s}{\beta_2 L} \quad \text{and} \quad g_{\max} = \frac{-\alpha + 2\gamma LP_s}{2L}, \quad (32)$$

where we considered ω_n as a continuous variable. We can thus interpret the condition $\mu_n = 0$ as a phase-matching relation that maximizes the energy transfer from the pump to the perturbations.

For the zero mode we have

$$\sigma(0) = \frac{-\alpha + \sqrt{(2\gamma LP_s(1 + G))^2 - (\phi_0 + 4(1 + G)\gamma LP_s)^2}}{t_R}. \quad (33)$$

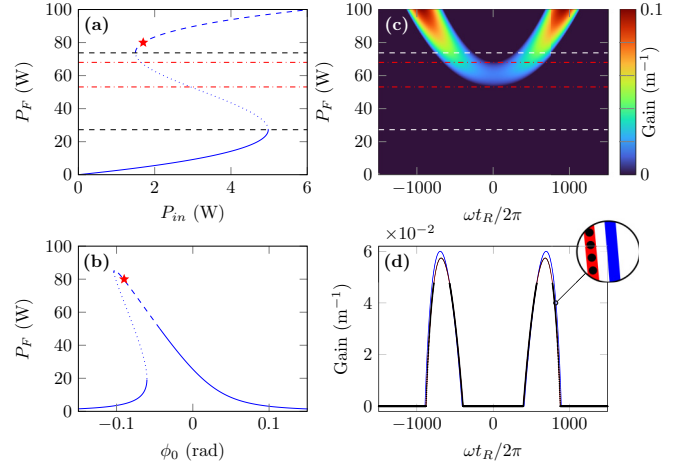


FIG. 4. (a) Steady states as a function of pump power at $\phi_0 = -0.09$ rad. (b) Steady states as a function of linear phase at $P_{in} = 1.7$ W. (c) Color level plot of gain $g(\omega)$ in the plane (ω, P_F) of frequency and forward intracavity power, calculated from Eq. (24). The dashed horizontal lines in (a) and (c) delimit the region of bistability, while dash-dotted horizontal lines delimit MI when $\omega_n \sim 0$. (d) Gain spectrum obtained from Eq. (A4) (black dots, Eq. (24) (red curve), and Eq. (31) (blue curve) for an intracavity power $P_F = 80$ W and $\phi_0 = -0.09$ rad; see red star in (a) and (b). Parameters: $\rho_1^2 = \rho_2^2 = 0.98$ ($\mathcal{F} = 156$), $\theta_1^2 = \theta_2^2 = 0.02$, $\gamma = 2 \text{ W}^{-1}/\text{km}$, $\beta_1 = c/1.5$, $\beta_2 = -20 \text{ ps}^2/\text{km}$, and $L = 0.1$ m.

The condition for reality of Eq. (33) coincides with the negative-slope branch of Eq. (26); i.e., the homogeneous solution is unstable if $P^- < P_s < P^+$, where

$$P^\pm = \frac{-2\phi_0 \pm \sqrt{\phi_0^2 - 3\alpha^2}}{6(1 + G)\gamma L}. \quad (34)$$

The unstable region obtained by letting $\omega_n \rightarrow 0$ in Eq. (31) is different and the limits are given by

$$\tilde{P}^\pm = \frac{-(2 + G)\phi_0 \pm \sqrt{\phi_0^2 - ((2 + G)^2 - 1)\alpha^2}}{2((2 + G)^2 - 1)\gamma L}. \quad (35)$$

Equations (35) and (34) coincide for $G = 0$, i.e., the ring cavity, where the instability of the homogeneous state coincides with the low-frequency limit of the modulationally unstable branch. This peculiarity of FP resonator was first pointed out in Ref. [17].

In order to illustrate the results of linear stability analysis of models in Eqs. (1) and (25), we consider for definiteness a fiber FP resonator, whose parameters are reported in Fig. 4. Figures 4(a) and 4(b) demonstrate examples of the intracavity steady-state power obtained from Eq. (7) as a function of pump power and linear phase cavity, respectively. The corresponding FP-LLE curves obtained from Eq. (26) are almost superimposed and they are not shown in order to make the figures more readable. As usual, the nonlinear phase shift acquired by the intracavity field does not impact the resonance width, but it does tilt the resonance [see Fig. 4(b)]. If input power and cavity finesse are high enough, the resonances become increasingly tilted, resulting in a multivalued cavity response. At certain values of ϕ_0 , the cavity can operate in a

bistable regime, as shown in Fig. 4(a). Figure 4(c) displays the gain of MI calculated from Eq. (24) for the anomalous GVD regime, as a function of the mode frequencies and the intracavity forward field power P_F . Also in this case the results obtained from FP-LLE [Eq. (26)] are practically identical (figure not shown). Modulationally unstable steady states are represented by a dashed curve in Figs. 4(a) and 4(b). Steady states which are unstable with respect to perturbations at zero frequency, corresponding to the negative-slope branch of the bistable response, are displayed in dotted curves. One noteworthy characteristic of the FP case is that the MI does not fully cover the cw unstable region, as it is the case for the ring cavity. Figure 4(d) exhibits an example of gain spectrum obtained from Eqs. (A4), (24), and (31). The agreement between the different methods is perfect, even if the cavity's finesse is not very high. This example shows that FP-LLE is a valuable tool for the description of MI in FP resonators. However, the mean-field model fails to describe some particular regimes, as it will be shown later.

IV. PULSED PUMP

A. Stationary periodic solutions

In this section we consider a pulsed pump with a repetition rate that matches the round-trip time, meaning that $E_{\text{in}}(t + t_R) = E_{\text{in}}(t)$ is a periodic function. Equations (1) and (2) can be analytically solved if dispersion is neglected ($\beta_2 = 0$) [10]. The solution can be written in implicit form as

$$\begin{aligned} F(z, t) &= F(0, t - \beta_1 z) \exp \left[i\gamma |F(0, t - \beta_1 z)|^2 z \right. \\ &\quad \left. + i\gamma G \int_0^z |B(s, t - \beta_1 z + \beta_1 s)|^2 ds \right], \\ B(z, t) &= B(0, t + \beta_1 z) \exp \left[-i\gamma |B(0, t + \beta_1 z)|^2 z \right. \\ &\quad \left. - i\gamma G \int_0^z |F(s, t + \beta_1 z - \beta_1 s)|^2 ds \right]. \end{aligned} \quad (36)$$

In the following we restrict our attention to a piecewise-constant (or quasi-cw) pump. We thus consider a train of rectangular-shaped pump pulses of duration $\Delta t = f_r t_R < t_R$ and constant amplitude E_{in0} :

$$E_{\text{in}}(t) = \begin{cases} E_{in0} & \text{if } n t_R < t < n t_R + f_r t_R \\ 0 & \text{elsewhere.} \end{cases} \quad (37)$$

Here, $f_r = \Delta t / t_R$ is the ratio between the pump pulse duration and the cavity round-trip time (i.e., the duty cycle), and we search for time-periodic (steady-state) solutions. In this case, Eqs. (36) can be calculated explicitly:

$$\begin{aligned} F(z, t) &= F_0 \exp[i\gamma(|F_0|^2 z + GX_F(z, t))] \\ &\quad \text{if } \beta_1 z + n t_R < t < \beta_1 z + n t_R + \Delta t, \\ B(z, t) &= B_0 \exp[-i\gamma(|B_0|^2 z + GX_B(z, t))] \\ &\quad \text{if } -\beta_1 z + n t_R < t < -\beta_1 z + n t_R + \Delta t, \end{aligned} \quad (38)$$

where F_0 and B_0 are complex constants to be determined, and

$$\begin{aligned} X_F(z, t) &= \int_0^z |B(s, t - \beta_1 z + \beta_1 s)|^2 ds, \\ X_B(z, t) &= \int_0^z |F(s, t + \beta_1 z - \beta_1 s)|^2 ds. \end{aligned} \quad (39)$$

The XPM terms $X_{F,B}$ are piecewise-linear functions in (z, t) . Their expressions are rather cumbersome, and reported in Appendix D (Table I or II depending whether $f_r < 0.5$ or $f_r > 0.5$). The complex constants of F_0 and B_0 are found by imposing boundary conditions (2). We find that F_0 and B_0 are still given by Eqs. (5), but with a different nonlinear phase shift:

$$\phi_{NL} = \gamma(1 + f_r G)(1 + \rho_2^2)|F_0|^2 L. \quad (40)$$

We see that the effect of periodic pumping is to reduce the XPM by a factor f_r . This is a peculiarity of the FP case: pumping the cavity with quasi-cw pulses does change the stationary states. For a ring resonator this effect is absent because $G = 0$. If the pulse duration is much shorter than the round-trip time ($f_r \ll 1$), the stationary states tend to the ones of a ring cavity.

B. Stability of quasi-cw solutions

We now consider the stability of the periodic solutions in Eqs. (38) with respect to dispersive perturbations ($\beta_2 \neq 0$). We assume that the forward and backward fields have the following form:

$$F(z, t) = F_p(z, t)(1 + f(z, t)), \quad (41a)$$

$$B(z, t) = B_p(z, t)(1 + b(z, t)), \quad (41b)$$

where F_p, B_p are the periodic solutions in Eqs. (38), f, b small perturbations, and we insert this ansatz in Eqs. (1). The inclusion of dispersion is not compatible with the discontinuous solutions in Eqs. (38), so we approximate the square pulse with a smooth flat-top pulse with a rise time which is much shorter than the pulse duration Δt , but long enough to neglect the dispersive effect on the stationary periodic solution. In practice, we neglect the terms $\beta_2 \frac{\partial F_p}{\partial t}$ and $\beta_2 \frac{\partial B_p}{\partial t}$ in the equations for the perturbations. Moreover, in the spirit of the approximation made in Sec. III B, we assume $G = 0$ in the equations for the perturbations. By expanding the perturbations as in Eqs. (11), we obtain again Eqs. (12), with the steady state given by Eqs. (5) and (40). Eventually, the MI gain can be still calculated with Eq. (24), which depends on the pulse duration through Eqs. (5) and (40).

Mean field

A similar analysis can be done also for the mean-field model. The steady periodic solution $\psi_p(t)$ of Eq. (25) with $\beta_2 = 0$ with square pulse pumping, Eq. (37), has the same temporal shape of the pump, with peak power P_p and constant phase. The power P_p is given by the following cubic equation:

$$\theta_1^2 P_{\text{in}} = P_p(\alpha^2 + (\phi_0 + 2\gamma L P_p(1 + f_r G))^2). \quad (42)$$

Again, we see that the effect of the pulsed pumping is to reduce the XPM coefficient G by a factor f_r . For a cw pump $f_r = 1$ and we recover Eq. (26).

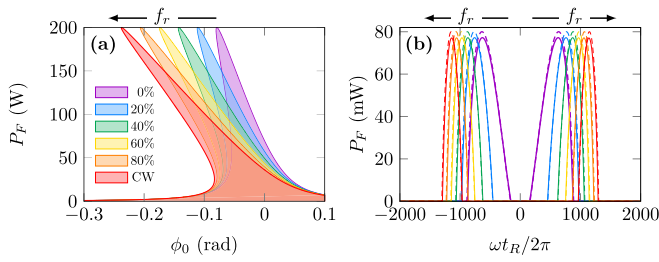


FIG. 5. (a) Steady states as a function of ϕ_0 for $P_{in} = 4$ W and different values of f_r from 0% to 100% (the arrow points to increasing values). (b) Gain spectrum obtained from Eq. (24) (solid curves) and FP-LLE (dashed curves) for an intracavity power $P_F = 90$ W and $\phi_0 = -0.04$ rad for different values of f_r . Cavity parameters: see Fig. 4.

We perform a linear stability by considering a perturbed solution of the form $\psi(t, \tau) = \psi_p(t) + \varepsilon_n(\tau)e^{i\omega_n t} + \varepsilon_{-n}(\tau)e^{-i\omega_n t}$ and include dispersion. As done in the previous section, we approximate the square pulse with a smooth flat-top pulse with a rise time much shorter than the pulse duration Δt , but long enough to minimize the dispersive effects on the stationary periodic solution. This way, we can neglect the term $\beta_2 \frac{\partial^2 \psi_p}{\partial t^2}$ in the equations for the perturbations. By following the procedure described in Sec. III C, and assuming $\int_0^{\Delta t} e^{i\omega_n t} dt \approx 0$ ($n \neq 0$), we find that the perturbations are ruled again by Eqs. (30) with the substitution $G \rightarrow f_r G$. At the end, the results of the stability analysis given by Eqs. (31)–(35) are still valid with G replaced by $f_r G$.

To illustrate the effect of the duration of the pump pulses, we consider the FP cavity used in Fig. 4 with pulsed pumping. Figure 5(a) presents the cavity response plotted as a function of linear phase for various pulse durations. It can be observed that, as the pulse duration increases, the resonance shape becomes more tilted. This phenomenon is not observed in ring cavities since the XPM effect is absent, which results in an unchanged resonance shape. This observation indicates that the pulse duration is a significant control parameter in FP cavities. To further emphasize this relationship, Fig. 5(b) shows the MI gain spectrum for different pulse durations while maintaining the intracavity power constant. Interestingly, it is noticed that the maximum gain remains constant regardless of pulse duration, but the corresponding frequency is dependent on it.

The results of linear stability analysis permit to predict the position of the unstable spectral bands even in the fully nonlinear regime, where an almost periodic train of pulses, i.e., a frequency comb, is generated. Figure 6 shows the results of the numerical solution of FP-LLE with a standard Fourier split-step method. The initial condition is a cw [Figs. 6(a) and 6(b)] or a periodic steady state [Figs. 6(c) and 6(d)] perturbed by a small random noise and it is propagated over 1000 round trips in order to reach a stable state. For a cw pump, we see in Fig. 6(a) that the field fills all the cavity (the time window extends from $-t_R/2$ to $t_R/2$) and is composed of a quasiperiodic sequence of short pulses (see inset). The spectrum is composed of several lines generated by cascaded four-wave mixing (FWM), and the position of the first sideband is perfectly predicted by the linear stability analysis (LSA; black dashed line). For a pulsed pump, we see in Fig. 6(c) that

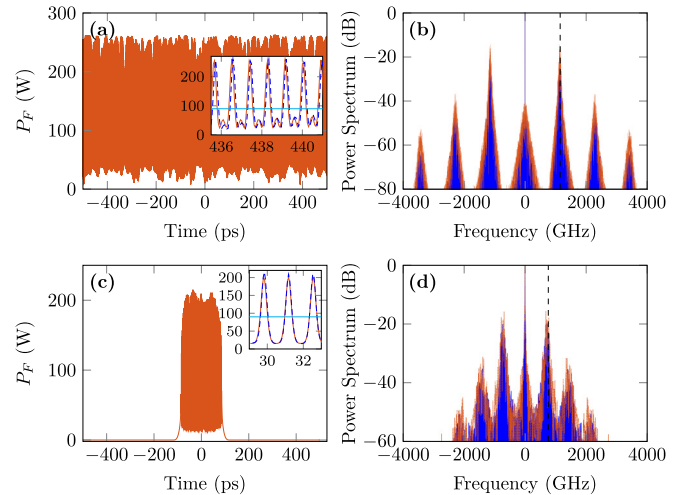


FIG. 6. Numerical simulations of MI-induced frequency comb generation for [(a), (b)] cw and [(c), (d)] pulsed pumping with $f_r = 0.2$. [(a), (c)] Intracavity power and [(b), (d)] spectrum after 1000 round trips. Orange curves correspond to FP-LLE, while blue curves correspond to the full model. The horizontal cyan line in the insets represents the input field. Black vertical dashed lines indicate the peak MI gain from Eq. (32): 1148 GHz in (b) and 759 GHz in (d). Initial intracavity power $P_F = 90$ W and $\phi_0 = -0.04$ rad; the rest of parameters are as in Fig. 4.

the cavity is partially empty. The field is composed of bursts of short pulses, as highlighted in the inset. The spectrum is still composed of several lines, but the spacing is different as predicted by the LSA (black dashed line). The experimental demonstration of these phenomena was recently published [32]. In Figs. 6(a)–(d) orange curves are the temporal and spectral traces obtained from the numerical solution of FP-LLE, while blue curves are obtained from coupled NLSEs. For the numerical solution of coupled NLSEs (1) and (2) we used a split-step, predictor-corrector method evolved in time [33]. We can see a very good agreement of the spectra in Figs. 6(b) and 6(d). The slight discrepancies are mainly due to the fact that the initial seed is random noise, which is not identical in the two simulations. The overall agreement of temporal traces in Figs. 6(a) and 6(c) is also good. The insets show a zoom on a limited temporal span, showing a remarkable quantitative agreement. The numerical simulation of FP-LLE took only 0.5 min on a standard workstation, while the full model took 9 h (1000 times slower) for the same number of round trips and the same frequency span. The long computation time for the coupled NLSEs is mainly caused by the counterpropagation, which imposes to solve two equations with two different group velocities. More specifically, the spatial and temporal grids are linked to each other by the Courant-Friedrichs-Lewy condition, which in our case gives $\Delta t = \beta_1 \Delta z$ because we integrate along the characteristics [33]. That means that once the spatial grid is fixed, the size of the numerical time step is also fixed and is typically a tiny fraction of the round-trip time. Conversely, for the FP-LLE the two grids are independent and, more importantly, the field evolves slowly, making it possible to massively reduce the number of time steps. The maximal size of the time step is

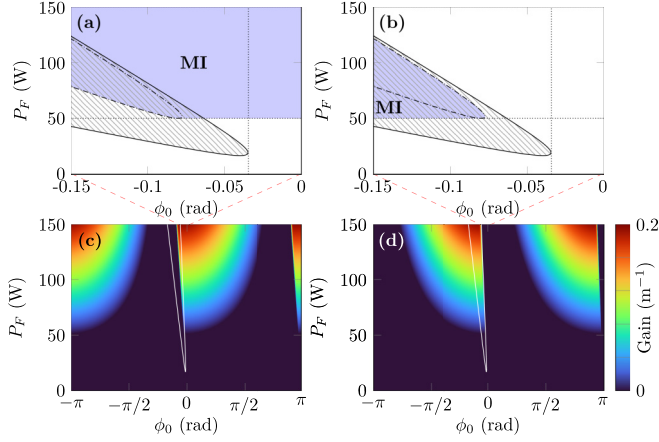


FIG. 7. Instability chart, obtained using [(a), (b)] the FP-LLE model and [(c), (d)] the full model in the (ϕ_0, P_F) plane for [(a), (c)] anomalous and [(b), (d)] normal GVD regimes. Modulationally unstable domains are shaded in blue and continuous-wave unstable domains are hatched. Solid curves correspond to P^\pm , which delimits the bistable region. Dash-dotted curves delimit the low-frequency limit of the MI unstable domains from Eqs. (35). Vertical dotted lines separate mono- and bistable regimes and the horizontal dotted lines show the threshold power P_{th} . Panels (c) and (d) show the two-dimensional map of the maximum gain for the full model from Eq. (24). Parameters as in Fig. 4.

typically imposed to avoid sideband instabilities typical of split-step methods [34].

V. LIMITATIONS OF THE MEAN-FIELD MODEL

The examples presented in the previous sections showed that FP-LLE permits to accurately reproduce the results of the full model. However, the derivation of FP-LLE involves approximations that result in inherent limitations. In order to identify the regions in the parameter space where the mean-field model breaks down, we draw a chart of instability from the results of LSA.

We start by considering FP-LLE. Modulation instability occurs when $g_{\max} > 0$, and using Eq. (32), we can derive the intracavity power threshold $P_{th} = \alpha/(2\gamma L)$, which is independent of ϕ_0 and the sign of the GVD parameter. Figure 7 illustrates the bistability and MI regions as a function of the cavity linear phase ϕ_0 , with hatched areas corresponding to the negative-slope branch of the bistable curve between P^- and P^+ from Eq. (34), blue area corresponding to the MI region, and white areas to the stable region. For $\beta_2 < 0$, MI arises in both bistable and monostable regimes when $P_F > P_{th}$, whereas for $\beta_2 > 0$, MI arises only in the bistable regime and is confined to a relatively small domain. The dash-dotted curve delimits the low-frequency limit of the MI unstable domains from Eqs. (35). It is worth noting that for certain values of (ϕ_0, P_F) in the bistable region, only the mode $\omega = 0$ is unstable, which is a distinguishing feature of FP cavities.

For the full model, the boundary between the stable and unstable regions is given by Eq. (19), which is the solution of the equation $g(\omega) = 0$ from Eq. (24). Figures 7(c) and 7(d) show the MI gain calculated from Eq. (24), over the full range of cavity linear phase $(-\pi, \pi)$. Differently than

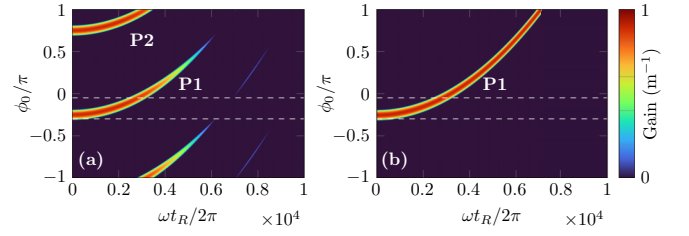


FIG. 8. Color level plot of gain $g(\omega)$ in the plane (ω, ϕ_0) of frequency and cavity linear phase (detuning), calculated from (a) Eq. (24) and (b) FP-LLE [Eq. (31)], with intracavity power $P_F = 500$ W. The dashed horizontal lines delimit an estimate of the region of validity of the LLE. Parameters as in Fig. 4.

FP-LLE, the MI power threshold does depend on ϕ_0 . In particular, both in the normal and the anomalous regimes, we can see two unstable tongues, one centered around zero detuning and the other around $\phi_0 = \pi$. The unstable region centered at $\phi = 0$ corresponds to even values of m in Eq. (23), meaning that the unstable frequencies correspond to cavity resonances $\omega t_R = 2n\pi$. However, the unstable region centered at $\phi = \pi$ corresponds to odd values of m in Eq. (23), meaning that the unstable frequencies $\omega t_R = (2n + 1)\pi$ are in between two resonances (antiresonance). We may identify in this second case the period-doubling (P2) MI, which has been described before for ring cavities [29,35–37]. The difference between standard (i.e., period one, P1) MI and P2 MI is that the modulations developing from the instability are in phase (P1) or shifted by half a temporal period (P2) at each round trip. It is worth noting that previous theoretical studies on P2 MI were based on the Ikeda map, which does not permit to resolve the cavity modes. As happens in ring resonators, the FP-LLE fails to predict P2 instabilities. To highlight this feature, we report in Fig. 8(a) the gain in (ω, ϕ_0) obtained from Eq. (24). The two instability branches are labeled P1 and P2 in the figure. The P1 instability is captured by FP-LLE, as shown in Fig. 8(b). On the other hand, the P2 instability is not visible in the gain calculated from FP-LLE.

In the following we complement the results of the linear stability analysis with numerical solution of the governing equations in the fully developed nonlinear regime. Figure 9 reports the generation of a P1 MI comb from numerical simulations of Eqs. (1) and (2) (blue curves) and FP-LLE in Eq. (25) (red curves). Figure 9(a) shows the output spectrum after 10 000 round trips, where a steady state is reached. The position of the unstable bands is well predicted by LSA ($f_{\max} = 1050$ GHz). Figure 9(b) shows a zoom of the temporal behavior of the intracavity field at the output mirror at round trip 10 000. The field is composed of an almost periodic train of short pulses, which reproduces itself at each round trip. Figures 9(a) and 9(b) show a good agreement between the full and mean-field models (blue and red curves). For this simulation, the computation time for the mean-field model was divided by around 1500 times with respect to the full model. Figure 9(c) shows a zoom of the spectrum around the maximum of the first band: only frequencies corresponding to the cavity resonances are excited, as predicted by LSA and shown in Fig. 9(d).

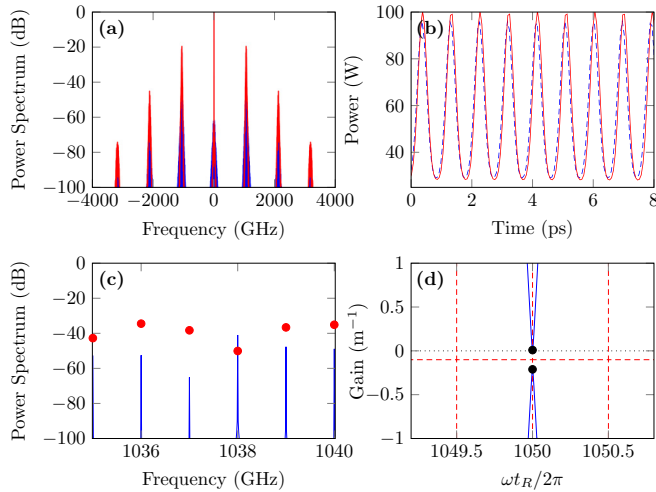


FIG. 9. (a) Output spectrum after 10000 round trips. Blue dashed and red solid curves correspond to the full model and FP-LLE. (b) Intracavity power at the output mirror as a function of normalized time $t - nt_R$, $n = 10000$. Blue dashed and red solid curves correspond to the full model and FP-LLE. (c) Zoom on the spectrum around the 1038th resonance (FSR = 1 GHz). Blue curve and red dots correspond to the full model and FP-LLE. (d) Graphical solution of Eq. (A4). $P_F = 50$ W, $\phi_0 = 0$. Rest of parameters as in Fig. 4. Simulation time around 23 h for the full model, 50 s for FP-LLE.

Figure 10 reports the generation of a P2 MI comb from numerical simulations of Eqs. (1) and (2). Figure 10(a) shows the output spectrum after 10000 round trips, where a steady state is reached. The position of the unstable bands is well predicted by LSA ($f_{\max} = 555$ GHz). Quite surprisingly, the first FWM band around $2f_{\max}$ is not generated, whereas the second

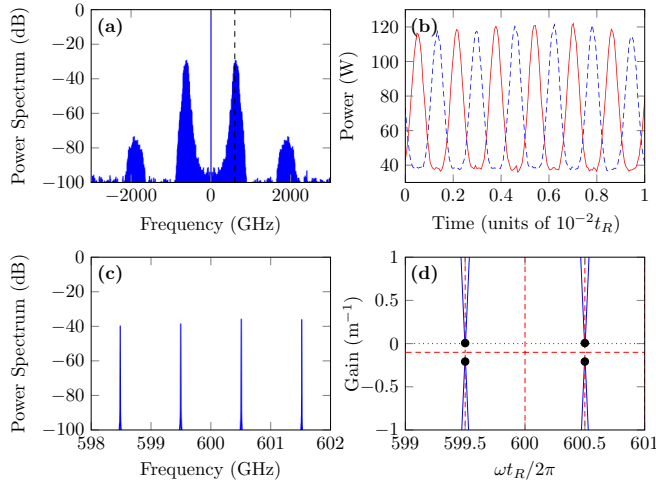


FIG. 10. (a) Output spectrum after 10000 round trips. Vertical dashed line is the maximally unstable frequency obtained from LSA. (b) Intracavity power at the output mirror as a function of normalized time $(t - nt_R)/t_R$, $n = 9999, 10000$. Blue dashed and red solid curves correspond to the round trips 9999 and 10000. (c) Zoom on the spectrum around the 600th resonance (FSR = 1 GHz). (d) Graphical solution of Eq. (A4). $P_F = 50$ W, $\phi_0 = 0.98\pi$. Rest of parameters as in Fig. 4. Simulation time around 20 h.

FWM band is clearly visible around $3f_{\max}$. Figure 10(c) shows a zoom of the spectrum around the maximum of the first band: the modes have frequencies which fall in between two adjacent cavity resonances, as predicted by LSA shown in Fig. 10(d).

This observation may explain why first-order FWM is not present. Indeed, the spectrum of the field is composed of lines at antiresonance. Frequency doubling of the first sideband will lead to lines at cavity resonances, which are inhibited in this configuration. The analysis of the features of the fully developed P2 MI pattern is still under investigation. Figure 10(b) shows the temporal behavior of the intracavity field at the output mirror at two consecutive round trips. We clearly see that the two traces are out of phase, the typical signature of P2 MI.

VI. CONCLUSION

We have studied modulation instability in Kerr Fabry-Perot cavities. Starting from a coupled NLSE description of the cavity dynamics, we have derived the exact dispersion relation for the perturbations and we found approximate analytical expressions for the instabilities threshold and gain spectrum of modulation instability. We showed that, in contrast to ring resonators, both the stationary solutions and the gain spectrum depend on the pump-pulse duration. We derived the extended Lugiato-Lefever equation for the Fabry-Perot resonator (FP-LLE) starting from coupled nonlinear Schrödinger equations and we compared the results of the stability analysis of the two models. While FP-LLE gives overall good results, we showed regimes that are not captured by the mean-field limit, namely, the period-two modulation instability, which may appear in highly detuned or nonlinear regimes. In the limit of vanishing dispersion, period doubling (Ikeda) instability may occur for homogeneous solutions [10], which leads to self-pulsing and the generation of square waves. This behavior, which is not captured by the mean-field approach, was studied recently in a particular Fabry-Perot resonator (Gires-Tournois interferometer) [38,39]. We reported numerical simulations of the generation of MI-induced Kerr combs by solving FP-LLE and the coupled NLSE. Overall, our study aims at gaining a deeper understanding of the nonlinear dynamics of Fabry-Perot cavities, which could have important implications for the development of new technologies and applications in fields such as telecommunications, optical sensing, and metrology. Our theory is a valuable support for the interpretation of some recent experiments in fiber resonators [20,32]. The findings of our study could potentially assist the design of more efficient and robust cavity-based systems.

ACKNOWLEDGMENTS

The present research was supported by the Agence Nationale de la Recherche (Programme Investissements d'Avenir, I-SITE VERIFICO) and IRCICA.

APPENDIX A: EXACT DISPERSION RELATION

The matrix differential equation (12) is linear and homogeneous, so it can be solved by standard methods (e.g.,

matrix exponential). However, the analytic expressions are very cumbersome since they depend on the roots of a general fourth-order polynomial. The eigenvalues η_j ($j = 1 - 4$) of \mathcal{M} are given by the roots of the characteristic polynomial

$$\eta_j^4 + a_2\eta_j^2 + a_1\eta_j + a_0 = 0, \quad (\text{A1})$$

where

$$a_2 = \frac{\beta_2^2}{2}\lambda^4 - 2\beta_1^2\lambda^2 - \gamma P_F(1 + \rho_2^2)\beta_2\lambda^2,$$

$$a_1 = 2\gamma P_F\beta_1\beta_2(1 - \rho_2^2)\lambda^3,$$

$$a_0 = \frac{\beta_2^4}{16}\lambda^8 + \frac{\beta_2^2}{4}(2\beta_1^2 - \gamma P_F(1 + \rho_2^2)\beta_2)\lambda^6$$

$$\mathcal{N} = \begin{pmatrix} (u_{1,1} - u_{1,3})e^{\eta_1 L} & (u_{2,1} - u_{2,3})e^{\eta_2 L} & (u_{3,1} - u_{3,3})e^{\eta_3 L} & (u_{4,1} - u_{4,3})e^{\eta_4 L} \\ (u_{1,2} - u_{1,4})e^{\eta_1 L} & (u_{2,2} - u_{2,4})e^{\eta_2 L} & (u_{3,2} - u_{3,4})e^{\eta_3 L} & (u_{4,2} - u_{4,4})e^{\eta_4 L} \\ u_{1,1} - \rho_1\rho_2e^{+i\phi}u_{1,3} & u_{2,1} - \rho_1\rho_2e^{+i\phi}u_{2,3} & u_{3,1} - \rho_1\rho_2e^{+i\phi}u_{3,3} & u_{4,1} - \rho_1\rho_2e^{+i\phi}u_{4,3} \\ u_{1,2} - \rho_1\rho_2e^{-i\phi}u_{1,4} & u_{2,2} - \rho_1\rho_2e^{-i\phi}u_{2,4} & u_{3,2} - \rho_1\rho_2e^{-i\phi}u_{3,4} & u_{4,2} - \rho_1\rho_2e^{-i\phi}u_{4,4} \end{pmatrix}. \quad (\text{A3})$$

In order to have a nontrivial solution, we must impose the determinant of \mathcal{N} to be zero, which yields

$$\det \mathcal{N} = C_{1,2}e^{(\eta_1+\eta_2)L} + C_{1,3}e^{(\eta_1+\eta_3)L} + C_{1,4}e^{(\eta_1+\eta_4)L} + C_{2,3}e^{(\eta_2+\eta_3)L} + C_{2,4}e^{(\eta_2+\eta_4)L} + C_{3,4}e^{(\eta_3+\eta_4)L} = 0, \quad (\text{A4})$$

where

$$\begin{aligned} C_{1,2} &= +[u_{3,1}u_{4,2} - u_{3,2}u_{4,1} + \rho_1^2\rho_2^2(u_{3,3}u_{4,4} - u_{3,4}u_{4,3}) - \rho_1\rho_2((u_{3,1}u_{4,4} - u_{3,4}u_{4,1})e^{-i\phi} - (u_{3,2}u_{4,3} - u_{3,3}u_{4,2})e^{+i\phi})]\sigma_{1,2}, \\ C_{1,3} &= -[u_{2,1}u_{4,2} - u_{2,2}u_{4,1} + \rho_1^2\rho_2^2(u_{2,3}u_{4,4} - u_{2,4}u_{4,3}) - \rho_1\rho_2((u_{2,1}u_{4,4} - u_{2,4}u_{4,1})e^{-i\phi} - (u_{2,2}u_{4,3} - u_{2,3}u_{4,2})e^{+i\phi})]\sigma_{1,3}, \\ C_{1,4} &= +[u_{2,1}u_{3,2} - u_{2,2}u_{3,1} + \rho_1^2\rho_2^2(u_{2,3}u_{3,4} - u_{2,4}u_{3,3}) - \rho_1\rho_2((u_{2,1}u_{3,4} - u_{2,4}u_{3,1})e^{-i\phi} - (u_{2,2}u_{3,3} - u_{2,3}u_{3,2})e^{+i\phi})]\sigma_{1,4}, \\ C_{2,3} &= +[u_{1,1}u_{4,2} - u_{1,2}u_{4,1} + \rho_1^2\rho_2^2(u_{1,3}u_{4,4} - u_{1,4}u_{4,3}) - \rho_1\rho_2((u_{1,1}u_{4,4} - u_{1,4}u_{4,1})e^{-i\phi} - (u_{1,2}u_{4,3} - u_{1,3}u_{4,2})e^{+i\phi})]\sigma_{2,3}, \\ C_{2,4} &= -[u_{1,1}u_{3,2} - u_{1,2}u_{3,1} + \rho_1^2\rho_2^2(u_{1,3}u_{3,4} - u_{1,4}u_{3,3}) - \rho_1\rho_2((u_{1,1}u_{3,4} - u_{1,4}u_{3,1})e^{-i\phi} - (u_{1,2}u_{3,3} - u_{1,3}u_{3,2})e^{+i\phi})]\sigma_{2,4}, \\ C_{3,4} &= +[u_{1,1}u_{2,2} - u_{1,2}u_{2,1} + \rho_1^2\rho_2^2(u_{1,3}u_{2,4} - u_{1,4}u_{2,3}) - \rho_1\rho_2((u_{1,1}u_{2,4} - u_{1,4}u_{2,1})e^{-i\phi} - (u_{1,2}u_{2,3} - u_{1,3}u_{2,2})e^{+i\phi})]\sigma_{3,4}, \end{aligned}$$

and

$$\sigma_{i,j} = (u_{i,1} - u_{i,3})(u_{j,2} - u_{j,4}) - (u_{j,1} - u_{j,3})(u_{i,2} - u_{i,4}).$$

APPENDIX B: MODULATION INSTABILITY IN A RING CAVITY WITH A TAP COUPLER

We consider a ring resonator composed of two spans of identical fiber connected to an input coupler 1 and a tap coupler 2, as illustrated in Fig. 2. If there is no coupling between forward and backward fields, it is easy to obtain a map that describes the behavior of the system at each round trip [40]. The fields propagating in the two spans satisfy NLSEs

$$i\frac{\partial F_n}{\partial z} - \frac{\beta_2}{2}\frac{\partial^2 F_n}{\partial t^2} + \gamma|F_n|^2F_n = 0, \quad 0 < z < L, \quad (\text{B1})$$

$$i\frac{\partial B_n}{\partial z} - \frac{\beta_2}{2}\frac{\partial^2 B_n}{\partial t^2} + \gamma|B_n|^2B_n = 0, \quad L < z < 2L, \quad (\text{B2})$$

and they are coupled by the following boundary conditions at couplers:

$$F_{n+1}(0, t) = \theta_1 E_{\text{in}} + \rho_1 e^{i\phi_0} B_n(2L, t), \quad (\text{B3})$$

$$B_n(L, t) = \rho_2 F_n(L, t). \quad (\text{B4})$$

$$+ (\beta_1^4 - \gamma P_F \beta_1^2 \beta_2 (1 + \rho_2^2) - \gamma^2 P_F^2 \rho_2^2 (G^2 - 1) \beta_2^2) \lambda^4.$$

The solution of Eqs. (12) can be expressed in terms of eigenvalues and eigenvectors of \mathcal{M} :

$$(f_+, f_-, b_+, b_-)^T = \sum_{j=1}^4 c_j e^{\eta_j z} \mathbf{u}_j, \quad (\text{A2})$$

where $\mathbf{u}_j = (u_{j,1}, u_{j,2}, u_{j,3}, u_{j,4})^T$ are the eigenvectors of \mathcal{M} . The four arbitrary constants c_j are determined by the boundary conditions.

Indeed, by inserting Eq. (A2) [identical to Eq. (14), reported here for clarity] in Eq. (13), we obtain a system of algebraic equations $\mathcal{N}(c_1, c_2, c_3, c_4)^T = 0$, where

The total linear phase ϕ_0 accounts for propagation and phase from the couplers and the index n counts the number of round trips.

1. Steady states

Steady-state solutions of Eqs. (B1) and (B2) read as

$$F_n(z, t) = F_0 e^{i\gamma P_F z}, \quad P_F = |F_0|^2, \quad (\text{B5})$$

$$B_n(z, t) = B_0 e^{i\gamma P_B z}, \quad P_B = |B_0|^2. \quad (\text{B6})$$

By using the boundary conditions, we find the cavity transfer function,

$$F_0 = \frac{\theta_1 E_{\text{in}}}{1 - \rho_1 \rho_2 \exp[i(\phi_0 + \phi_{NL})]}, \quad (\text{B7})$$

which permits to write the input power $P_{\text{in}} = |E_{\text{in}}|^2$ as a function of intracavity forward power $P_F = |F_0|^2$ as

$$P_{\text{in}} = \frac{P_F}{\theta_1^2} (1 + (\rho_1 \rho_2)^2 - 2\rho_1 \rho_2 \cos(\theta_0)), \quad (\text{B8})$$

with $\theta_0 = \phi_0 + \phi_{NL} = \phi_0 + \gamma P_F L (1 + \rho_2^2)$.

It is worth noting that Eq. (B7) is equivalent to the steady state of a FP resonator with $G = 0$ and it is also equivalent to the steady state of a ring resonator of length $2L$ if $\rho_2 = 1$.

2. Linear stability analysis

We consider a perturbation of the steady state in the following form:

$$F_n(z, t) = (\sqrt{P_F} + \eta)e^{i\gamma P_F z}, \quad (\text{B9})$$

$$B_n(z, t) = (\rho_2 \sqrt{P_F} + \varepsilon)e^{i\gamma \rho_2^2 P_F z} e^{i\gamma \phi_B}, \quad (\text{B10})$$

where we have assumed without loss of generality F_0 real, which fixes the phase $\phi_B = \gamma L P_F (1 - \rho_2^2)$ through boundary condition (B4). Linearization around steady solutions gives the equations for the perturbations:

$$i\eta_z - \frac{\beta_2}{2}\eta_{tt} + \gamma P_F(\eta + \eta^*) = 0, \quad (\text{B11})$$

$$i\varepsilon_z - \frac{\beta_2}{2}\varepsilon_{tt} + \gamma \rho_2^2 P_F(\varepsilon + \varepsilon^*) = 0. \quad (\text{B12})$$

We split perturbations into real and imaginary parts, $\eta = a + ib$ and $\varepsilon = c + id$, and we substitute into Eqs. (B11) and (B12) and Fourier transform to get

$$\begin{pmatrix} \hat{a} \\ \hat{b} \end{pmatrix}_z = \begin{pmatrix} 0 & -\frac{\beta_2 \omega^2}{2} \\ \frac{\beta_2 \omega^2}{2} + 2\gamma P_F & 0 \end{pmatrix} \begin{pmatrix} \hat{a} \\ \hat{b} \end{pmatrix},$$

$$\begin{pmatrix} \hat{c} \\ \hat{d} \end{pmatrix}_z = \begin{pmatrix} 0 & -\frac{\beta_2 \omega^2}{2} \\ \frac{\beta_2 \omega^2}{2} + 2\gamma \rho_2^2 P_F & 0 \end{pmatrix} \begin{pmatrix} \hat{c} \\ \hat{d} \end{pmatrix}. \quad (\text{B13})$$

The fundamental matrix solutions of systems (B13) are

$$M(z) = \begin{pmatrix} \cos kz & -\frac{\beta_2 \omega^2}{2k} \sin kz \\ \frac{2k}{\beta_2 \omega^2} \sin kz & \cos kz \end{pmatrix}, \quad (\text{B14})$$

$$N(z) = \begin{pmatrix} \cos k_\rho z & -\frac{\beta_2 \omega^2}{2k_\rho} \sin k_\rho z \\ \frac{2k_\rho}{\beta_2 \omega^2} \sin k_\rho z & \cos k_\rho z \end{pmatrix}, \quad (\text{B15})$$

with k, k_ρ defined in Eqs. (16) with $P = P_F$ and $\lambda = i\omega$. The boundary conditions give the following relations:

$$\begin{pmatrix} \hat{c}_n(L) \\ \hat{d}_n(L) \end{pmatrix} = \rho_2 \begin{pmatrix} \hat{a}_n(L) \\ \hat{b}_n(L) \end{pmatrix},$$

$$\begin{pmatrix} \hat{a}_{n+1}(0) \\ \hat{b}_{n+1}(0) \end{pmatrix} = \rho_1 \begin{pmatrix} \cos \theta_0 & -\sin \theta_0 \\ \sin \theta_0 & \cos \theta_0 \end{pmatrix} \begin{pmatrix} \hat{c}_n(2L) \\ \hat{d}_n(2L) \end{pmatrix}. \quad (\text{B16})$$

By combining propagation and boundary conditions, we get the following difference equation:

$$\begin{pmatrix} \hat{a}_{n+1}(0) \\ \hat{b}_{n+1}(0) \end{pmatrix} = S \begin{pmatrix} \hat{a}_n(0) \\ \hat{b}_n(0) \end{pmatrix}, \quad S = \rho_1 \rho_2 R N(L) M(L), \quad (\text{B17})$$

and R is the rotation matrix defined in Eq. (B16).

The eigenvalues $\lambda_{1,2}$ of matrix S determine the stability of the steady solution. We find

$$\lambda_{1,2} = \frac{\tilde{\Delta}}{2} \pm \sqrt{\frac{\tilde{\Delta}^2}{4} - |\rho_1 \rho_2|^2}, \quad (\text{B18})$$

with $\tilde{\Delta}$ as defined in Eq. (20). Instability takes places if $|\lambda_{1,2}| > 1$ and the MI gain is

$$g(\omega) = \frac{1}{2L} \ln \max \left| \frac{\tilde{\Delta}}{2} \pm \sqrt{\frac{\tilde{\Delta}^2}{4} - |\rho_1 \rho_2|^2} \right|, \quad (\text{B19})$$

which coincides with the gain for the FP resonator found before in Eq. (24).

APPENDIX C: FP-LLE DERIVATION

We derive a mean-field model, which generalizes the Lugiato-Lefever equation, for the description of a passive driven fiber Fabry-Perot cavity. We follow an approach similar to the one developed in Ref. [17] but with a different starting point, namely, coupled NLSEs [Eqs. (1) and (2)] rather than Maxwell-Bloch equations. While Maxwell-Bloch equations are more general, they are not routinely used in the nonlinear fiber-optics community, where the characteristic parameters of the fibers (group velocity dispersion, nonlinear coefficient, etc.) can be directly plugged into NLSEs. The main steps are (i) changing variables to make the boundary conditions periodic and to include the pump term in the propagation equation, (ii) taking the good-cavity (or mean-field) approximation, and (iii) deriving a partial differential equation using the modal equations. We start by defining the following change of variables [1,41]:

$$\begin{aligned} \tilde{F}(z, t) &= \exp \left[\frac{z-L}{L} \left(\ln \rho_1 + i \frac{\phi_0}{2} \right) - \nu z \right] F(z, t) \\ &+ \frac{\theta_1}{\rho_1} \exp \left(-i \frac{\phi_0}{2} \right) \frac{z-L}{2L} E_{\text{in}}(t - \beta_1 z), \end{aligned} \quad (\text{C1a})$$

$$\begin{aligned} \tilde{B}(z, t) &= \exp \left[-\frac{z}{L} \left(\ln \rho_2 + i \frac{\phi_0}{2} \right) - \nu z - i \frac{\phi_0}{2} \right] B(z, t) \\ &- \frac{\theta_1}{\rho_1} \exp \left(-i \frac{\phi_0}{2} \right) \frac{z-L}{2L} E_{\text{in}}(t + \beta_1 z), \end{aligned} \quad (\text{C1b})$$

with $\nu = \frac{1}{2L} \ln(\rho_1/\rho_2)$. This transformation is more general than the one proposed in Refs. [1,41] because we allow the two mirrors to be different and the pump may vary in time. The boundary conditions given by Eqs. (2) for the new variables are simplified to

$$\begin{aligned} \tilde{F}(0, t) &= \tilde{B}(0, t), \\ \tilde{F}(L, t) &= \tilde{B}(L, t). \end{aligned} \quad (\text{C2})$$

The simplification of the boundary conditions is paid for by an increase in complexity of the propagation equations. We thus restrict our analysis to good cavities ($\rho_{1,2} \rightarrow 1$ and $\phi_0 \rightarrow 0$), for which we can obtain a mean-field description. From Eqs. (C1) we calculate $\partial_z F$, $\partial_t F$, $\partial_z B$, $\partial_t B$ as a function of \tilde{F} , \tilde{B} and their derivatives. We truncate the obtained expressions at first order in $\rho_{1,2}$ and ϕ_0 and insert them into Eqs. (1). By considering that dispersion and nonlinearity are

weak (assumptions already used to derive NLSEs), we can use zero-order expansion ($\tilde{F} = F$, $\tilde{B} = B$) in the dispersive and nonlinear terms. These approximations permit to greatly simplify the propagation equations as follows:

$$\frac{\partial \tilde{F}}{\partial z} + \beta_1 \frac{\partial \tilde{F}}{\partial t} + i \frac{\beta_2}{2} \frac{\partial^2 \tilde{F}}{\partial t^2} - \frac{1}{L} \left(\frac{\ln \rho_1 \rho_2}{2} + i \frac{\phi_0}{2} \right) \tilde{F} - \frac{\theta_1}{2L} E_{\text{in}}(t - \beta_1 z) = i\gamma (|\tilde{F}|^2 + G|\tilde{B}|^2) \tilde{F}, \quad (\text{C3a})$$

$$-\frac{\partial \tilde{B}}{\partial z} + \beta_1 \frac{\partial \tilde{B}}{\partial t} + i \frac{\beta_2}{2} \frac{\partial^2 \tilde{B}}{\partial t^2} - \frac{1}{L} \left(\frac{\ln \rho_1 \rho_2}{2} + i \frac{\phi_0}{2} \right) \tilde{B} - \frac{\theta_1}{2L} E_{\text{in}}(t + \beta_1 z) = i\gamma (|\tilde{B}|^2 + G|\tilde{F}|^2) \tilde{B}. \quad (\text{C3b})$$

1. Modal equations

We start by finding the modes of the empty and undriven (cold) cavity; then we expand the fields of the hot cavity in terms of the modes of the cold cavity and derive the equations ruling the slow evolution of the modal amplitudes. By taking $\beta_2 = \phi_0 = E_{\text{in}} = \gamma = 0$, we solve Eqs. (C3) with boundary conditions (C2), to find

$$\tilde{F}(z, t) = A \exp \left[\left(\beta_1 \lambda + \frac{\ln \rho_1 \rho_2}{2L} \right) z \right] e^{-\lambda t}, \quad (\text{C4a})$$

$$\tilde{B}(z, t) = A \exp \left[- \left(\beta_1 \lambda + \frac{\ln \rho_1 \rho_2}{2L} \right) z \right] e^{-\lambda t}, \quad (\text{C4b})$$

with

$$\exp[2\beta_1 \lambda L + \ln(\rho_1 \rho_2)] = 1, \quad (\text{C5})$$

where A and λ are constants. By defining $\lambda = \kappa + i\omega$, we get from Eq. (C5)

$$\omega_m = \frac{m\pi}{\beta_1 L} \quad \text{and} \quad \kappa = -\frac{\ln(\rho_1 \rho_2)}{2\beta_1 L}, \quad (\text{C6})$$

which are the frequencies and the decay rate of the cavity modes. We may write the modes of the cold cavity as

$$\tilde{F}_m(z, t) = e^{-\kappa t} e^{-i\omega_m(t - \beta_1 z)}, \quad (\text{C7a})$$

$$\tilde{B}_m(z, t) = e^{-\kappa t} e^{-i\omega_m(t + \beta_1 z)}. \quad (\text{C7b})$$

The fields in the full model can now be written as the sum of the lossless cold cavity modes, allowing for a slow temporal variation of the modal amplitudes, which is induced by pumping, nonlinear, and dispersive effects. Note that the small damping κ is also accounted for in the slowly varying modal amplitudes. We thus may write

$$\tilde{F}(z, t) = \sum_m a_m(t) e^{-i\omega_m(t - \beta_1 z)}, \quad (\text{C8a})$$

$$\tilde{B}(z, t) = \sum_m a_m(t) e^{-i\omega_m(t + \beta_1 z)}. \quad (\text{C8b})$$

We consider a periodic input, synchronized with the cavity repetition rate, which can be expanded in Fourier series as follows:

$$E_{\text{in}}(t) = \sum_m S_m e^{-i\omega_m t}. \quad (\text{C9})$$

We insert Eqs. (C8) and (C9) in Eq. (C3a), multiply by $e^{i\omega_n(t - \beta_1 z)}$, and integrate in $z \in [-L, L]$ to obtain

$$\begin{aligned} & \beta_1 \dot{a}_n - \left(\frac{\ln(\rho_1 \rho_2)}{2L} + i \frac{\phi_0}{2L} \right) a_n \\ & + i \frac{\beta_2}{2} (\ddot{a}_n - 2i\omega_n \dot{a}_n - \omega_n^2 a_n) - \frac{\theta_1}{2L} S_n \\ & = i\gamma \sum_{n', n''} a_{n'} a_{n''}^* (a_{n-n'+n''} + G a_{n+n'-n''}) e^{-2i(\omega_{n'} - \omega_{n''})t}. \end{aligned} \quad (\text{C10})$$

We assume that the modal amplitudes change slowly over a round trip, i.e., $|\dot{a}_n| \ll |\omega_n a_n|$. This assumption permits to simplify the dispersive contribution, by neglecting the time derivatives of the modal amplitudes in the third term of Eq. (C10). Moreover, by integrating Eq. (C10) in time over one round trip, and considering $a_n(t)$ constant in this range, the fast oscillations in the second nonlinear term are averaged out. We eventually obtain

$$\begin{aligned} & \dot{a}_n + \left(\kappa - i \frac{\phi_0}{2\beta_1 L} - i \frac{\beta_2}{2\beta_1} \omega_n^2 \right) a_n - \frac{\theta_1}{2\beta_1 L} S_n \\ & = i \frac{\gamma}{\beta_1} \left(\sum_{n', n''} a_{n'} a_{n''}^* a_{n-n'+n''} + G a_n \sum_{n'} |a_{n'}|^2 \right). \end{aligned} \quad (\text{C11})$$

The same equation is also obtained by following a similar procedure starting from Eq. (C3b).

2. Mean-field FP-LLE

We may now define the slowly varying envelope of the forward and backward fields in the laboratory frame as

$$\psi(z, t) = \sum_m a_m(t) e^{-i\omega_m t} e^{i\beta_1 \omega_m z}, \quad (\text{C12a})$$

$$\psi_B(z, t) = \sum_m a_m(t) e^{-i\omega_m t} e^{-i\beta_1 \omega_m z}. \quad (\text{C12b})$$

It is apparent that the fields are periodic in space of period $2L$ and they satisfy $\psi(z, t) = \psi_B(-z, t)$. Thanks to this relation we can relate the fields in the “nonphysical” cavity $-L < z < 0$ to the real cavity $0 < z < L$ to their counterpropagating counterparts [17]. By using

$$\frac{\partial \psi}{\partial t} = \sum_m (\dot{a}_m(t) - i\omega_m a_m) e^{-i\omega_m t} e^{i\beta_1 \omega_m z},$$

$$\frac{\partial^n \psi}{\partial z^n} = \sum_m (i\beta_1 \omega_m)^n a_m(t) e^{-i\omega_m t} e^{i\beta_1 \omega_m z},$$

we easily get

$$\begin{aligned} & \frac{\partial \psi}{\partial t} + \frac{1}{\beta_1} \frac{\partial \psi}{\partial z} + \left(\kappa - i \frac{\phi_0}{2\beta_1 L} \right) \psi \\ & + i \frac{\beta_2}{2\beta_1^3} \frac{\partial^2 \psi}{\partial z^2} - \frac{\theta_1}{2\beta_1 L} E_{\text{in}}(t - \beta_1 z) \\ & = i \frac{\gamma}{\beta_1} \left(|\psi|^2 + \frac{G}{2L} \int_{-L}^L |\psi(z', t)|^2 dz' \right) \psi. \end{aligned} \quad (\text{C13})$$

By means of the change of variable $z \rightarrow -z + t/\beta_1 \pmod{2L}$ and multiplying by the round-trip time $t_R = 2\beta_1 L$

TABLE I. Cross-phase terms for $f_r < 0.5$.

$f_r < 0.5$			
Time interval	Space interval	$X_F(z, t)$	$X_B(z, t)$
$0 < t < \frac{t_R}{2} f_r$	$0 < z < \frac{t}{\beta_1}$	$ B_0 ^2 z$	$ F_0 ^2 z$
	$\frac{t}{\beta_1} < z < 2f_r L - \frac{t}{\beta_1}$	0	$ F_0 ^2 (\frac{z}{2} + \frac{t}{2\beta_1})$
$\frac{t_R}{2} f_r < t < t_R f_r$	$2f_r L - \frac{t}{\beta_1} < z < L$	0	0
	$0 < z < 2f_r L - \frac{t}{\beta_1}$	$ B_0 ^2 z$	$ F_0 ^2 z$
$t_R f_r < t < \frac{t_R}{2}$	$2f_r L - \frac{t}{\beta_1} < z < \frac{t}{\beta_1}$	$ B_0 ^2 (\frac{z}{2} - \frac{t}{2\beta_1} + f_r L)$	0
	$\frac{t}{\beta_1} < z < L$	0	0
$\frac{t_R}{2} < t < \frac{t_R}{2} (1 + f_r)$	$0 < z < \frac{t}{\beta_1} - 2f_r L$	0	0
	$\frac{t}{\beta_1} - 2f_r L < z < \frac{t}{\beta_1}$	$ B_0 ^2 (\frac{z}{2} - \frac{t}{2\beta_1} + f_r L)$	0
$\frac{t_R}{2} < t < \frac{t_R}{2} (1 + f_r)$	$\frac{t}{\beta_1} < z < L$	0	0
	$0 < z < \frac{t}{\beta_1} - 2f_r L$	0	0
$\frac{t_R}{2} (1 + f_r) < t < t_R (\frac{1}{2} + f_r)$	$\frac{t}{\beta_1} - 2f_r L < z < 2L - \frac{t}{\beta_1}$	$ B_0 ^2 (\frac{z}{2} - \frac{t}{2\beta_1} + f_r L)$	0
	$2L - \frac{t}{\beta_1} < z < L$	$ B_0 ^2 (z - L(1 - f_r))$	$ F_0 ^2 (z - L(1 - f_r))$
$t_R (\frac{1}{2} + f_r) < t < t_R$	$0 < z < 2L - \frac{t}{\beta_1}$	0	0
	$2L - \frac{t}{\beta_1} < z < \frac{t}{\beta_1} - 2f_r L$	0	$ F_0 ^2 (\frac{z}{2} + \frac{t}{2\beta_1} - L)$
$t_R (\frac{1}{2} + f_r) < t < t_R$	$\frac{t}{\beta_1} - 2f_r L < z < L$	$ B_0 ^2 (z - L(1 - f_r))$	$ F_0 ^2 (z - L(1 - f_r))$
	$0 < z < 2L - \frac{t}{\beta_1}$	0	0
$t_R (\frac{1}{2} + f_r) < t < t_R$	$2L - \frac{t}{\beta_1} < z < 2L(1 + f_r) - \frac{t}{\beta_1}$	0	$ F_0 ^2 (\frac{z}{2} + \frac{t}{2\beta_1} - L)$
	$2L(1 + f_r) - \frac{t}{\beta_1} < z < L$	0	0

we get

$$\begin{aligned} t_R \frac{\partial \psi}{\partial t} = & -(\alpha - i\phi_0)\psi - 2iL \frac{\beta_2}{2\beta_1^2} \frac{\partial^2 \psi}{\partial z^2} + \theta_1 E_{\text{in}}(\beta_1 z) \\ & + 2iL\gamma \left(|\psi|^2 + \frac{G}{2L} \int_{-L}^L |\psi(z', t)|^2 dz' \right) \psi, \end{aligned} \quad (\text{C14})$$

where $\alpha = \kappa t_R = -\ln(\rho_1 \rho_2) \approx 1 - \rho_1 \rho_2$. This form of FP-LLE reduces to the one obtained by Cole *et al.* [17] for the case of cw pumping and identical mirrors. Its structure is usual in the context of microresonators [42]. More precisely, the evolution is in time and the transverse dimension is the space with periodic boundary conditions.

In fiber ring resonators it is customary to have evolution in space (also called slow time) and a temporal transverse coordinate [31,43]. The role of time and space can be swapped at first order if we consider that the most important effect is the translation at the group velocity [44,45]. Indeed, in Eq. (C13) the first two terms are of order one, while the remaining ones are first-order corrections. This means that, at the lowest order, we have

$$\frac{\partial \psi}{\partial z} \approx -\beta_1 \frac{\partial \psi}{\partial t} \quad \text{and} \quad \frac{\partial^2 \psi}{\partial z^2} \approx \beta_1^2 \frac{\partial^2 \psi}{\partial t^2}. \quad (\text{C15})$$

By using the second of the relations above in Eq. (C13) and making the change of variable $t \rightarrow t - \beta_1 z$, we get the space-propagated version of the FP-LLE,

$$\begin{aligned} 2L \frac{\partial \psi}{\partial z} = & -(\alpha - i\phi_0)\psi - iL\beta_2 \frac{\partial^2 \psi}{\partial t^2} + \theta_1 E_{\text{in}}(t) \\ & + 2i\gamma L \left(|\psi|^2 + \frac{G}{t_R} \int_{-t_R/2}^{t_R/2} |\psi(z, t')|^2 dt' \right) \psi, \end{aligned} \quad (\text{C16})$$

where $z > 0$ and $-t_R/2 < t < t_R/2$. Even if Eq. (C16) and Eq. (C13) have the same degree of approximation, only the time-propagated version has the correct boundary conditions. Indeed, in Eq. (C16) we have assumed that the field is periodic in time, which is not strictly true. This also implies that the modes have a constant frequency spacing (FSR), while in reality the FSR changes slightly because of dispersion. Conversely, in Eq. (C14) the modes have equally spaced wave numbers, but their frequencies are fixed by the dispersion relation. These facts are almost irrelevant in standard (i.e., “long,” tens of meters) fiber ring resonators, because the round-trip time is usually much longer than the pulse circulating in the resonator. This usually allows one to consider an infinite round-trip time with constant boundary conditions. The field is no longer considered periodic and its spectrum, which is now continuous, gives the envelope of the discrete spectrum of the full optical field circulating in the cavity.

APPENDIX D: EXACT SOLUTION FOR SQUARE PULSE PUMPING

In this section we report the explicit expressions of the cross-phase modulation terms in Eqs. (39), for $t \in [0, t_R]$, given the periodicity of the functions. The expressions are different depending if the duty cycle f_r of the square pulse is greater or lesser than 0.5. The fundamental period $[0, t_R]$ is divided into six intervals, where functions (39) have different forms. For each time interval, there exist three different spatial intervals where functions (39) are different in general. Tables I and II report the explicit expressions of Eqs. (39) for $f_r < 0.5$ and $f_r > 0.5$.

TABLE II. Cross-phase terms for $f_r > 0.5$.

$f_r > 0.5$			
Time interval	Space interval	$X_F(z, t)$	$X_B(z, t)$
$0 < t < t_R(f_r - \frac{1}{2})$	$0 < z < \frac{t}{\beta_1}$	$ B_0 ^2 z$	$ F_0 ^2 z$
	$\frac{t}{\beta_1} < z < \frac{t}{\beta_1} + 2L(1 - f_r)$	0	$ F_0 ^2(\frac{z}{2} + \frac{t}{2\beta_1})$
$t_R(f_r - \frac{1}{2}) < t < \frac{t_R}{2} f_r$	$\frac{t}{\beta_1} + 2L(1 - f_r) < z < L$	$ B_0 ^2(z - L(1 - f_r))$	$ F_0 ^2(z - L(1 - f_r))$
	$0 < z < \frac{t}{\beta_1}$	$ B_0 ^2 z$	$ F_0 ^2 z$
$\frac{t_R}{2} f_r < t < \frac{t_R}{2}$	$\frac{t}{\beta_1} < z < 2f_r L - \frac{t}{\beta_1}$	0	$ F_0 ^2(\frac{z}{2} + \frac{t}{2\beta_1})$
	$2f_r L - \frac{t}{\beta_1} < z < L$	0	0
$\frac{t_R}{2} < t < t_R f_r$	$0 < z < 2f_r L - \frac{t}{\beta_1}$	$ B_0 ^2 z$	$ F_0 ^2 z$
	$2f_r L - \frac{t}{\beta_1} < z < \frac{t}{\beta_1}$	$ B_0 ^2(\frac{z}{2} - \frac{t}{2\beta_1} + f_r L)$	0
$t_R f_r < t < \frac{t_R}{2}(1 + f_r)$	$\frac{t}{\beta_1} < z < L$	0	0
	$0 < z < 2f_r L - \frac{t}{\beta_1}$	$ B_0 ^2 z$	$ F_0 ^2 z$
$\frac{t_R}{2}(1 + f_r) < t < t_R$	$2f_r L - \frac{t}{\beta_1} < z < 2L - \frac{t}{\beta_1}$	$ B_0 ^2(\frac{z}{2} - \frac{t}{2\beta_1} + f_r L)$	0
	$2f_r L - \frac{t}{\beta_1} < z < L$	$ B_0 ^2(z - L(1 - f_r))$	$ F_0 ^2(z - L(1 - f_r))$
$\frac{t_R}{2}(1 + f_r) < t < t_R$	$0 < z < \frac{t}{\beta_1} - 2f_r L$	0	0
	$\frac{t}{\beta_1} - 2f_r L < z < 2L - \frac{t}{\beta_1}$	$ B_0 ^2(\frac{z}{2} - \frac{t}{2\beta_1} + f_r L)$	0
$\frac{t_R}{2}(1 + f_r) < t < t_R$	$2L - \frac{t}{\beta_1} < z < L$	$ B_0 ^2(z - L(1 - f_r))$	$ F_0 ^2(z - L(1 - f_r))$
	$0 < z < 2L - \frac{t}{\beta_1}$	0	0
$\frac{t_R}{2}(1 + f_r) < t < t_R$	$2L - \frac{t}{\beta_1} < z < \frac{t}{\beta_1} - 2f_r L$	0	$ F_0 ^2(\frac{z}{2} + \frac{t}{2\beta_1} - L)$
	$\frac{t}{\beta_1} - 2f_r L < z < L$	$ B_0 ^2(z - L(1 - f_r))$	$ F_0 ^2(z - L(1 - f_r))$

[1] L. Lugiato, F. Prati, and M. Brambilla, *Nonlinear Optical Systems* (Cambridge University Press, Cambridge, U.K., 2015)

[2] K. Ikeda, *Opt. Commun.* **30**, 257 (1979).

[3] W. Firth and C. Paré, *Opt. Lett.* **13**, 1096 (1988).

[4] W. Firth, C. Penman, and C. Paré, *Opt. Commun.* **75**, 136 (1990).

[5] W. Firth, A. Fitzgerald, and C. Paré, *J. Opt. Soc. Am. B* **7**, 1087 (1990).

[6] W. Firth and C. Penman, *Opt. Commun.* **94**, 183 (1992).

[7] J. B. Geddes, R. A. Indik, J. V. Moloney, and W. J. Firth, *Phys. Rev. A* **50**, 3471 (1994).

[8] C. Law and A. Kaplan, *Opt. Lett.* **14**, 734 (1989).

[9] C. Law and A. E. Kaplan, *J. Opt. Soc. Am. B* **8**, 58 (1991).

[10] W. Firth, *Opt. Commun.* **39**, 343 (1981).

[11] E. Abraham, W. Firth, and J. Carr, *Phys. Lett. A* **91**, 47 (1982).

[12] Y. Silberberg and I. Bar-Joseph, *J. Opt. Soc. Am. B* **1**, 662 (1984).

[13] M. Yu, C. McKinstrie, and G. P. Agrawal, *J. Opt. Soc. Am. B* **15**, 607 (1998).

[14] M. Yu, C. McKinstrie, and G. P. Agrawal, *J. Opt. Soc. Am. B* **15**, 617 (1998).

[15] W. J. Firth, J. B. Geddes, N. J. Karst, and G.-L. Oppo, *Phys. Rev. A* **103**, 023510 (2021).

[16] G. J. Morales and Y. C. Lee, *Phys. Rev. Lett.* **33**, 1016 (1974); K. Nozaki and N. Bekki, *Phys. Lett. A* **102**, 383 (1984); D. J. Kaup and A. C. Newell, *Phys. Rev. B* **18**, 5162 (1978).

[17] D. C. Cole, A. Gatti, S. B. Papp, F. Prati, and L. Lugiato, *Phys. Rev. A* **98**, 013831 (2018).

[18] D. Braje, L. Hollberg, and S. Diddams, *Phys. Rev. Lett.* **102**, 193902 (2009).

[19] E. Obrzud, S. Lecomte, and T. Herr, *Nat. Photonics* **11**, 600 (2017).

[20] T. Bunel, M. Conforti, Z. Ziani, J. Lumeau, A. Moreau, A. Fernandez, O. Llopis, J. Roul, A. M. Perego, K. K. Wong *et al.*, *Opt. Lett.* **48**, 275 (2023).

[21] K. Jia, X. Wang, D. Kwon, J. Wang, E. Tsao, H. Liu, X. Ni, J. Guo, M. Yang, X. Jiang *et al.*, *Phys. Rev. Lett.* **125**, 143902 (2020).

[22] Z. Xiao, T. Li, M. Cai, H. Zhang, Y. Huang, C. Li, B. Yao, K. Wu, and J. Chen, *Light Sci. Appl.* **12**, 33 (2023).

[23] M. Nie, K. Jia, Y. Xie, S. Zhu, Z. Xie, and S.-W. Huang, *Nat. Commun.* **13**, 6395 (2022).

[24] Z. Xiao, K. Wu, T. Li, and J. Chen, *Opt. Express* **28**, 14933 (2020).

[25] T. Wildi, M. A. Gaafar, T. Voumard, M. Ludwig, and T. Herr, *Optica* **10**, 650 (2023).

[26] G. N. Campbell, L. Hill, P. Del’Haye, and G.-L. Oppo, *Phys. Rev. A* **108**, 033505 (2023).

[27] K. Ogusu, H. Li, and T. Kamizono, *Opt. Rev.* **5**, 185 (1998).

[28] We found it more convenient to calculate the eigenvectors of matrix \mathcal{M} numerically. In order to avoid numerical instabilities, we have used the MATLAB built-in function `eig` by explicitly choosing the algorithm used, i.e., `[V,D] = eig(M,eye(4),'chol')`.

[29] M. Conforti, F. Copie, A. Mussot, A. Kudlinski, and S. Trillo, *Opt. Lett.* **41**, 5027 (2016).

[30] L. A. Lugiato and R. Lefever, *Phys. Rev. Lett.* **58**, 2209 (1987).

[31] M. Haelterman, S. Trillo, and S. Wabnitz, *Opt. Lett.* **17**, 745 (1992).

- [32] T. Bunel, Z. Ziani, M. Conforti, J. Lumeau, A. Moreau, A. Fernandez, O. Llopis, G. Bourcier, A. Perego, and A. Mussot, *Opt. Lett.* **48**, 5955 (2023).
- [33] C. Sun, N. Mangan, M. Dong, H. G. Winful, S. T. Cundiff, and J. N. Kutz, *J. Opt. Soc. Am. B* **36**, 3263 (2019).
- [34] F. Matera, A. Mecozzi, M. Romagnoli, and M. Settembre, *Opt. Lett.* **18**, 1499 (1993).
- [35] M. Haelterman, *Opt. Lett.* **17**, 792 (1992).
- [36] S. Coen and M. Haelterman, *Phys. Rev. Lett.* **79**, 4139 (1997).
- [37] F. Bessin, F. Copie, M. Conforti, A. Kudlinski, A. Mussot, and S. Trillo, *Phys. Rev. X* **9**, 041030 (2019).
- [38] E. R. Koch, T. G. Seidel, S. V. Gurevich, and J. Javaloyes, *Opt. Lett.* **47**, 4343 (2022).
- [39] M. Stöhr, E. R. Koch, J. Javaloyes, S. V. Gurevich, and M. Wolfrum, *Chaos* **33**, 113105 (2023).
- [40] D. Zezyulin, V. Konotop, and M. Taki, *Opt. Lett.* **36**, 4623 (2011).
- [41] L. Lugiato and L. Narducci, *Z. Phys. B* **71**, 129 (1988).
- [42] Y. K. Chembo and C. R. Menyuk, *Phys. Rev. A* **87**, 053852 (2013).
- [43] S. Coen, H. G. Randle, T. Sylvestre, and M. Erkintalo, *Opt. Lett.* **38**, 37 (2013).
- [44] A. Chabchoub and R. H. Grimshaw, *Fluids* **1**, 23 (2016).
- [45] *Rogue and Shock Waves in Nonlinear Dispersive Media*, edited by M. Onorato, S. Residori, and F. Baronio (Springer, Heidelberg, 2016), p. 10.